LETTERS
SPACE PHYSICS

Earth and Planetary Physics
2: 455–461, 2018
doi: 10.26464/epp2018043

Magnetic field data processing methods of the China Seismo-Electromagnetic Satellite

Bin Zhou[1*], YanYan Yang[2], YiTeng Zhang[1], XiaoChen Gou[1], BingJun Cheng[1], JinDong Wang[1], and Lei Li[1*]

[1]State Key Laboratory of Space Weather, National Space Science Center, Chinese Academy of Sciences, Beijing 100190, China;

[2]Institute of Crustal Dynamics, China Earthquake Administration, Beijing 100085, China

Abstract: The High Precision Magnetometer (HPM) on board the China Seismo-Electromagnetic Satellite (CSES) allows highly accurate measurement of the geomagnetic field; it includes FGM (Fluxgate Magnetometer) and CDSM (Coupled Dark State Magnetometer) probes. This article introduces the main processing method, algorithm, and processing procedure of the HPM data. First, the FGM and CDSM probes are calibrated according to ground sensor data. Then the FGM linear parameters can be corrected in orbit, by applying the absolute vector magnetic field correction algorithm from CDSM data. At the same time, the magnetic interference of the satellite is eliminated according to ground-satellite magnetic test results. Finally, according to the characteristics of the magnetic field direction in the low latitude region, the transformation matrix between FGM probe and star sensor is calibrated in orbit to determine the correct direction of the magnetic field. Comparing the magnetic field data of CSES and SWARM satellites in five continuous geomagnetic quiet days, the difference in measurements of the vector magnetic field is about 10 nT, which is within the uncertainty interval of geomagnetic disturbance.

Keywords: China Seismo-Electromagnetic Satellite (CSES); High Precision Magnetometer (HPM); fluxgate magnetometer; CPT magnetometer; data processing

Citation: Zhou, B., Yang, Y. Y., Zhang, Y. T., Gou, X. C., Cheng, B. J., Wang, J. D., and Li, L. (2018). Magnetic field data processing methods of the China Seismo-Electromagnetic Satellite. *Earth Planet. Phys.*, *2*(6), 455–461. http://doi.org/10.26464/epp2018043

1. Introduction

Utilizing low Earth orbit satellites to measure the magnetic field of the Earth is an important means for geomagnetic exploration. At present the mainstream geomagnetic models are all based on satellite magnetic field data. Satellite magnetic data processing solves mainly problems of sensor linear correction, residual magnetic interference, and vector orientation; the processing method depends on the size of target magnetic field and the payload configuration and platform features, and requires specific design.

If the target magnetic field is relatively weak and the requirement for data processing is relatively low, the linear correction is generally done by using ground calibration data, and the temperature drift is handled by linearization. However, at low Earth orbit altitude, the Earth's magnetic field is in the range from 20000 nT to 60000 nT, while the requirements for magnetic field resolution differs by 4–5 orders of magnitude between that from magnetic field fine structure and that from the space environment; this raises very strict requirements for satellite platforms, payloads, and data processing. All the low Earth orbit magnetic satellites in the world, such as MAGSAT, ORSTED, CHAMP, and SWARM, are equipped with scalar as well as vector fluxgate magnetometers (Potemra et al., 1980; Olsen et al., 2003; Merayo et al., 2000; Friis-Christensen et al., 2006). In addition, they also make linear corrections of the vector magnetic field data by some algorithm utilizing accurate scalar magnetic data based on characteristic atomic parameters, thus greatly improving the accuracy of vector magnetic data (Merayo et al., 2000; Yin F, 2010).

Magnetic data processing should also handle the issues of platform interference and coordinate transformation. All the magnetic satellites pay great attention to the influence of remnant magnetism; and magnetic cleanness control and configuration optimization are made to reduce the interference; on the other hand, ground magnetic measurement is carried out to assess its impact (Chen SW, 2009; Zhou B and Wang JD, 2013; Xiao Q et al., 2018). When the target magnetic field is relatively weak or if magnetic cleanness control is relatively good, linear correction based on ground test data can be used. The determination of the vector magnetic field direction is generally based on satellite attitude measurement; the precision of near-Earth magnetic field direction is generally required to be better than 0.01 degrees; accordingly, in data processing the measurement error of the star sensor and the impact of thermal deformation on the coordinate transformation matrix should be considered.

The CSES is a low Earth orbit satellite, with geomagnetic field measurement as one of its main scientific tasks (Shen XH et al., 2018). According to the task and platform characteristics, the HPM includes FGM (Fluxgate Magnetometer) and CDSM (Coupled Dark State Magnetometer) probes, designed to be used with specific

Correspondence to: B. Zhou, zhoubin@nssc.ac.cn
L. Li, lil@nssc.ac.cn
Received 23 AUG 2018; Accepted 10 OCT 2018.
Accepted article online 28 NOV 2018.

in-orbit data processing methods (Zhou B, 2013). HPM data collected during the satellite's commissioning phase, after its launch on February 2, 2018, were processed using ground calibration results (Cheng BJ, 2018). The processing method has been found to be robust and appropriate to produce high quality magnetic field data. The details are presented in this paper.

2. HPM Data Processing

The high precision magnetometer of CSES consists of two FGM and one CDSM probes, as shown in Figure1.

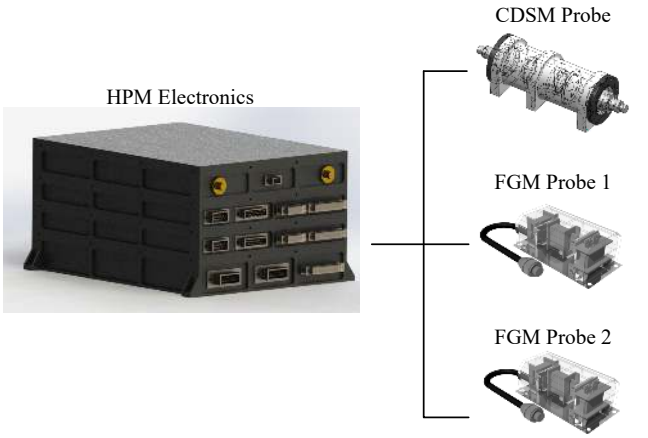

Figure 1. Schematic of HPM, consisting of two FGM probes, one CDSM probes and an electronics box.

The FGM probe consists of three single-component sensors, based on Faraday's electromagnetic induction law, arrayed orthogonally to constitute a vector magnetic sensor. The probe's data are processed mainly to solve the problems of thermal drift of the instrument gain factors and offsets, as well as the orthogonality problem of its three components. The scalar data from the CPT effect-based CDSM sensor can be used for FGM sensor linear correction; in principle the accuracy of scalar data is guaranteed (Lammegger, 2008). The actual in-orbit assessments of the HPM's major specifications are listed in Table 1.

Table 1. HPM performance in-orbit

Item		Performance
FGM	Range	±70000 nT
	Frequency band	15 Hz
	Resolution	0.09 nT
	Noise	18 pT·Hz$^{-1/2}$@1 Hz
	Linearity	0.004%
	Gain drift	20 ppm/℃
	Offset drift	0.05 nT/℃
	Offset stability	1 nT/Month
CDSM	Range	100000 nT
	Noise	29.9 pT·Hz$^{-1/2}$@1Hz
	Accuracy	0.19 nT
Vector magnetic field data precision	Magnitude	0.5 nT
	Orientation	0.05°

The data needed in data processing are listed in Table 2, they are mainly from three sources.

(1) In-orbit observations from the FGM and CDSM sensors, temperature data inside the FGM probes and electronic box, star sensor data, attitude data, and platform housekeeping parameters.

(2) Ground calibration data of the HPM, including temperature correction curves, the basic linear parameters of the fluxgate sensor, and the heading error correction parameters of the CDSM.

(3) Platform test data, mainly including the magnetic field induced by the platform at the CDSM sensor, the magnetic induction coefficient, and the payload installation matrix.

The processing of HPM data is divided into three main stages. The first stage is correction at the sensor level: the 6 components of the 2 FGM probes and the CDSM probe are corrected for factors such as temperature. Then FGM linear parameters correction fol-

Table 2. Required data list in HPM data processing

No.	Item	Symbol	Source
1.	Magnetic field from FGM	F_1, F_2	In-orbit measurement
2	Magnetic field from CDSM	S	In-orbit measurement
3	HPM temperature	t_{p1}, t_{p2}, t_e	In-orbit measurement
4	Star sensor attitude data	Q	In-orbit measurement
5	Orientation vector of magnetic torque	I	In-orbit measurement
6	Gain drift correction charts for FGM	$A_{T1}, A_{T2},$	HPM calibration
7	Offset drift correction charts for FGM	$C_{T1}, C_{T2},$	HPM calibration
8	Heading error correction curve for CDSM	H	HPM calibration
9	Interference matrix between sensor	$\boldsymbol{M}_{12}, \boldsymbol{M}_{21}, \boldsymbol{M}_{2c}$	HPM calibration
10	Transformation matrix from FGM to star sensor	$\boldsymbol{M}_{ps}$	Satellite test
11	Interference parameters from satellite	$\boldsymbol{M}_A, \boldsymbol{M}_B, \boldsymbol{M}_C$	Satellite test

lows, using the absolute vector magnetic field correction algorithm based on CDSM data; other interferences are also eliminated at this stage. The third stage is coordinate system transformation—from the sensor coordinate system to the physical coordinate system as required by users. This last stage is very important for the magnetic field data to be of optimum use.

2.1. Sensor Correction

2.1.1 Temperature correction of the FGM sensors

Theoretically, the raw signal observed by FGM sensors F is linearly related to the magnetic field. Taking the x component of FGM Probe 1 (F_{1x}) as an example, it is related to the magnetic field as shown by equation (1):

$$B_{1x} = aF_{1x} + c, \tag{1}$$

where B_{1x} is the magnetic field, in nT, observed by the x component of the fluxgate sensor after physical quantity transformation. According to the principle of FGM, gain factor a and offset c will change with temperature t. Ground calibration indicates that a drifts at a rate of 20 ppm/℃, while c is about 0.05 nT/℃, which is not negligible in the near Earth orbit environment. At the same time, these two parameters also change with the temperature of the electronics box. The temperature correction chart for each coefficient of the HPM sensor is obtained via ground calibration, such as shown by Figure 2 (Zhou B et al., 2018).

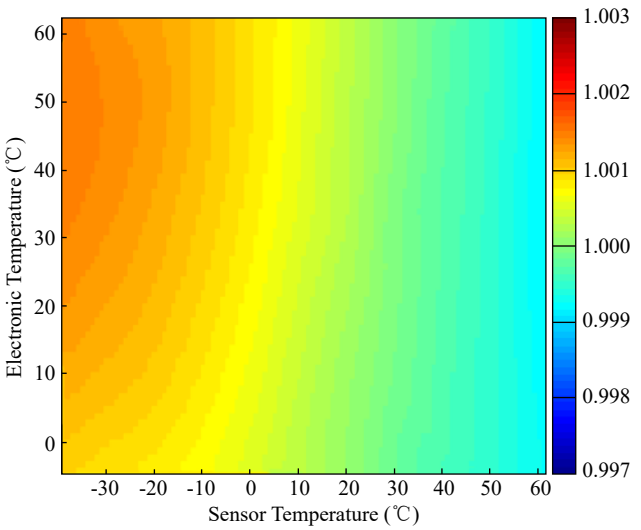

Figure 2. Linear coefficient thermal drift results: Gain factor, after interpolating with both sensor thermal drift and electronics thermal drift of FGM sensor 1x.

The final correction result can be obtained by interpolation of electronics temperature t_e and sensor temperature t_p. The temperature correction of the FGM sensor is shown in equation (2):

$$B_{1x} = A_{T1x}(t_e, t_{p1})F_{1x} + C_{T1x}(t_e, t_{p1}). \tag{2}$$

2.1.2 CDSM heading error correction

Theoretically, the measurement error caused by Zeeman nonlinear frequency shift of the Rb^{87} atom can be eliminated utilizing signal superposition produced by the double CPT effect of the CDSM. However the change of the angle between magnetic field direction and probe laser incidence direction will still produce small measurement errors, which can be accurately determined and corrected by ground calibration (Pollinger et al., 2018).

During the in-orbit operation of the satellite, the overall operation temperature of the CDSM sensor and its electronics box is very stable, the measurement error being mainly related to the direction of the magnetic field. Generally the data from FGM Probe 2, which is closer to the CDSM, are used as the input for determining magnetic field direction; the correction formula for the CDSM sensor is expressed as

$$B_s = aS - H(B_{2x}, B_{2y}, B_{2z}). \tag{3}$$

2.2. Linear Correction of Vector Magnetic Field

2.2.1 Absolute vector magnetic field correction algorithm

During the development of the CSES, methods by which accurate scalar magnetic data could be used to correct the vector magnetic field data of FGM were studied (Zhang ZQ et al., 2014). An algorithm was developed and verified by numerical simulation. The basic principle of this method is the mathematical relation between vector and scalar quantities, as shown by equation (4):

$$B_s^2 = B_X^2 + B_Y^2 + B_Z^2, \tag{4}$$

where B_X, B_Y, and B_Z represent the three-component magnetic field in an orthogonal coordinate system. The FGM sensor is not strictly orthogonal, and the gain factor and offset calibrated on the ground may change slightly in orbit; therefore, the B_x, B_y, and B_z from the FGM are mathematically related to the orthogonal 3-component magnetic field by equation (5):

$$\begin{bmatrix} B_X \\ B_Y \\ B_Z \end{bmatrix} = M(\theta_{xy}, \theta_{yz}, \theta_{xz}) \left(\begin{bmatrix} a_x & 0 & 0 \\ 0 & a_y & 0 \\ 0 & 0 & a_z \end{bmatrix} \begin{bmatrix} B_x \\ B_y \\ B_z \end{bmatrix} + \begin{bmatrix} b_x \\ b_y \\ b_z \end{bmatrix} \right). \tag{5}$$

Utilizing equations (4) and (5) simultaneously gives the mathematical relation between the scalar magnetic data and the vector magnetic field data, which includes 9 parameters to be solved. The solution can be obtained by fitting multiple observation data. The conditions of data fitting are as follows.

(1) The fitting data evenly cover the whole magnetic sphere (a unit sphere in the B_x, B_y, B_z coordinate system).

(2) The vector sensors and scalar sensor observe the same magnetic field.

(3) The parameters of the vector sensor are stable and do not change.

(4) The data from scalar sensor are accurate.

The CSES is a 3-axis stabilized platform, with a sun-synchronous orbit. Under the FGM probe coordinate system on the satellite, the distribution of observed magnetic field data on the magnetic sphere is shown in Figure 3. In principle, the in-orbit data can satisfy the requirements of the algorithm. The coverage on axis B_y and B_z (approximately the Earthward and forward direction of the satellite) is satisfied; however, the coverage on the B_x axis is not good enough. As a result, larger fitting errors in parameters re-

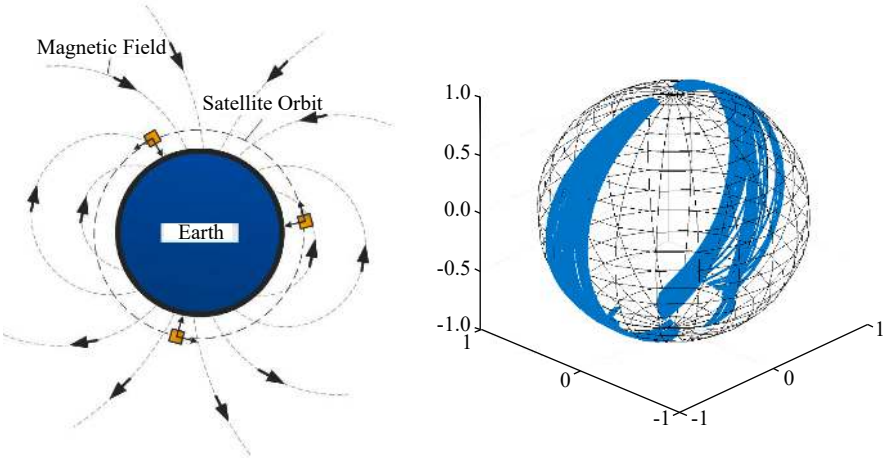

Figure 3. Global geomagnetic vector direction coverage of CSES. Left: Satellite orientation relative to the geomagnetic field; Right: Normalized geomagnetic vector in the FGM probe coordinates.

lated to B_x axis are expected.

Payload performance assessment indicated that the stability of vector magnetic observations is within 0.5 nT, and the accuracy of the scalar value can reach 0.19 nT; these meet the requirements of the algorithm. As long as the data from different sensors are normalized in data processing, all the algorithm conditions can be satisfied.

2.2.2 Interference elimination

Before its launch, CSES was operated with several magnetic tests, in which the effects of satellite residual magnetism, magnetic induction, and magnetic torque were measured. The magnetic interference produced by the satellite at the CDSM sensor is about 0–3 nT with an uncertainty of 0.26 nT (Xiao Q et al., 2018). The magnetic field, produced by the satellite, at the tip of the boom is approximated as that of a dipole; its interference decays with cubic distance, so the interference fields at FGM Probe 1 and FGM Probe 2 are all greater than that at the CDSM probe.

The FGM sensor includes a feedback coil, which reduces to zero the magnetic field inside the sensor, at the same time it produces a magnetic field outside. Mutual interference tests between the sensors of the HPM were carried out on ground, which found that, under the present configuration of the sensors, the interference on the neighboring sensor is about 0–2 nT.

Therefore, the three probes of HPM are situated in a superimposed magnetic field of space ambient field, satellite interference field, and sensor interference field. Figure 4 is a schematic diagram of this superimposed magnetic field.

$$\begin{cases} B_1 = B_{\text{space}} + B_{\text{sat}->\text{FGM1}} + B_{\text{FGM2}->\text{FGM1}} \\ B_2 = B_{\text{space}} + B_{\text{sat}->\text{FGM2}} + B_{\text{FGM1}->\text{FGM2}} \\ B_c = B_{\text{space}} + B_{\text{sat}->\text{CDSM}} + B_{\text{FGM2}->\text{CDSM}} \\ B_{\text{sat}->\text{FGM1}} : B_{\text{sat}->\text{FGM2}} : B_{\text{sat}->\text{CDSM}} = 1/L_1^3 : 1/L_2^3 : 1/L_c^3 \end{cases}$$
$$\Rightarrow \begin{cases} B_c = B_1 - B_{\text{FGM2}->\text{FGM1}} + B_{\text{sat}->\text{CDSM}} - \left(L_c^3/L_1^3 - 1\right) B_{\text{sat}->\text{CDSM}} \\ B_c = B_2 - B_{\text{FGM1}->\text{FGM2}} + B_{\text{sat}->\text{CDSM}} - \left(L_c^3/L_2^3 - 1\right) B_{\text{sat}->\text{CDSM}} \end{cases} \quad (6)$$

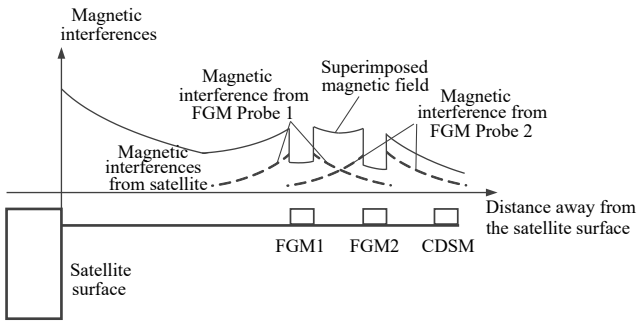

Figure 4. The influences of remanence of S/C are reduced with the distance increase, and the FGM feedback coils generate the magnetic interferences outside around too. The disturbances measured by HPM sensors are accumulation both from the S/C remanence and FGM feedback interferences.

The CDSM data are scalar and do not need vector processing. The magnetic field at the FGM sensor is extended to the position of the CDSM—see equation (6). Based on these data the absolute vector magnetic field correction is applied to get the linear parameters of the FGM. After correction, the FGM data represent the vector magnetic field at the CDSM sensor, which is further processed with equation (7) to get the ambient space magnetic field.

$$B_{\text{space}} = B_c - B_{\text{sat}->\text{CDSM}} - B_{\text{FGM2}->\text{CDSM}}. \quad (7)$$

The normalization processing also includes synchronization of vector and scalar data. The sample rate of the FGM data is 60 Hz and that of CDSM is 30 Hz; the time difference of the two raw records is about 10 ms. The average variation of the Earthward component of the geomagnetic field is 40 nT/s with a maximum up to 80 nT/s; a time difference of 10 ms may cause a magnetic field bias close to 1 nT, which should not be neglected in the processing.

2.2.3 Result of FGM linear correction

Absolute vector magnetic field correction can greatly improve the accuracy of in-orbit vector data. Figure 5 compares the scalar differences of raw FGM data, FGM data corrected with ground calibration coefficients, and FGM data corrected by using the in-orbit

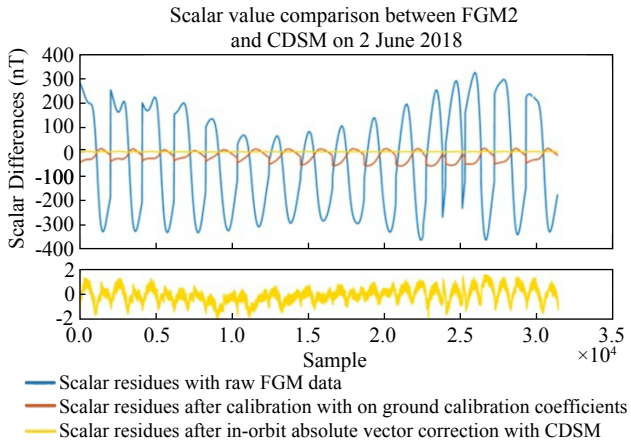

Figure 5. Scalar residual errors of sensor FGM2, compared under different corrections.

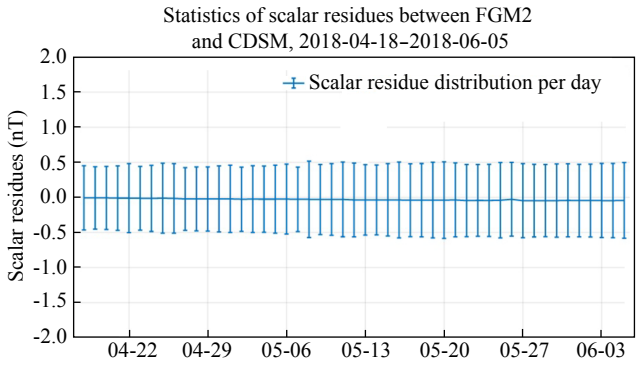

Figure 6. Temporal variation of fitting residuals of scalar magnetic field of FGM2.

absolute vector magnetic field correction method with CDSM. The residual error of FGM data corrected by the in-orbit absolute vector field is only 0±0.5 nT. Figure 6 shows the results on 50 consecutive days, indicating that the algorithm using CDSM scalar data to correct FGM vector magnetic data suits the in-orbit data very well and produces stable results.

Table 3 lists the statistic evaluation result of 9 linear parameters on 50 consecutive days. It can be seen that the linear parameters are also very stable.

2.3. Coordinate System Transformation

Considering the differences between ground and in-orbit conditions, the transformation matrix of FGM to star sensor is determined by in-orbit fitting. Utilizing the magnetic field relation at the intersection of ascending and descending orbits and the diurnal variation features of the magnetic field, the matrix can be determined. Transforming the magnetic data to the star sensor coordinate system, the star sensor attitude quaternion characterizes the transformation matrix between the star sensor coordinate system and the inertial coordinate system; the magnetic data can then be further transformed to the inertial coordinate system, as shown by equation (8):

$$B_{\text{intertial}} = M(Q)\, M_{\text{FGM}->\text{ss}} B_{\text{FGM}}. \quad (8)$$

Table 3. Statistics of linear correction parameters of FGM2

	Evaluated value	Uncertainty
X gain factor	1.0025461	0.0000573
Y gain factor	1.0008000	0.0000020
Z gain factor	1.0003115	0.0000095
Angle between *X* & *Y* (°)	89.3484	0.0005
Angle between *Y* & *Z* (°)	91.1107	0.0012
Angle between *Z* & *X* (°)	90.6544	0.0022
X offset (nT)	2.00	0.54
Y offset (nT)	–6.70	0.24
Z offset (nT)	–2.17	0.22

The transformation from inertial coordinate system to Earth-fixed coordinate system depends on time and the rotation of the Earth. The transformation matrix is calculated according to the IAU-2000/2006 precession and nutation model (Liu JC and Zhu Z., 2012) and data acquisition time. The data are then transformed to the Earth-fixed coordinate system. Further transformation from the Earth-fixed coordinate system to other coordinate systems, such as the North-East-Down geographic coordinate system and geomagnetic coordinate system, is relatively simple and will not be elaborated here.

3. Analysis of Data Processing Results

According to the definition of satellite data level, the corrected data from sensors, which represent just the physical values observed by the sensors, are Level 1 data. The data after orthogonality correction and coordinate transformation are Level 2 data, which represent the space magnetic field at the position of the satellite. Evaluation of the final result of data processing can be made by comparing Level 2 data with data from other magnetic measuring satellites in the ionosphere.

SWARM is a triple-satellite constellation for magnetic field measurement, with a vector field accuracy of 0.5 nT. The orbit altitude of the SWARM B satellite is 530 km (Friis-Christensen et al, 2006), close to the altitude of CSES, so its data are used for comparison.

Figure 8 shows the geomagnetic field observed by the CSES in a 5-day re-visiting period from May 19 to May 24 in 2018. As shown in Figure 7, the *Dst* index was very stable during those days, making this period favorable for data comparison. At the orbit intersection points of these two satellites, the data are neither time synchronous nor at the same altitude. Therefore, before the comparison they are normalized using the geomagnetic model

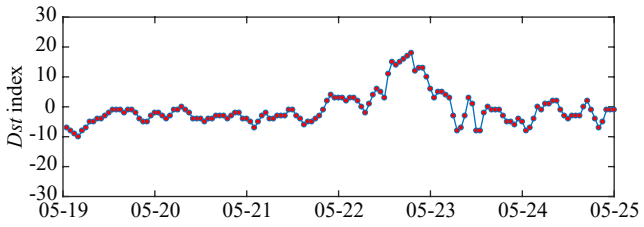

Figure 7. *Dst* index from May 19, 2018 to May 24, 2018.

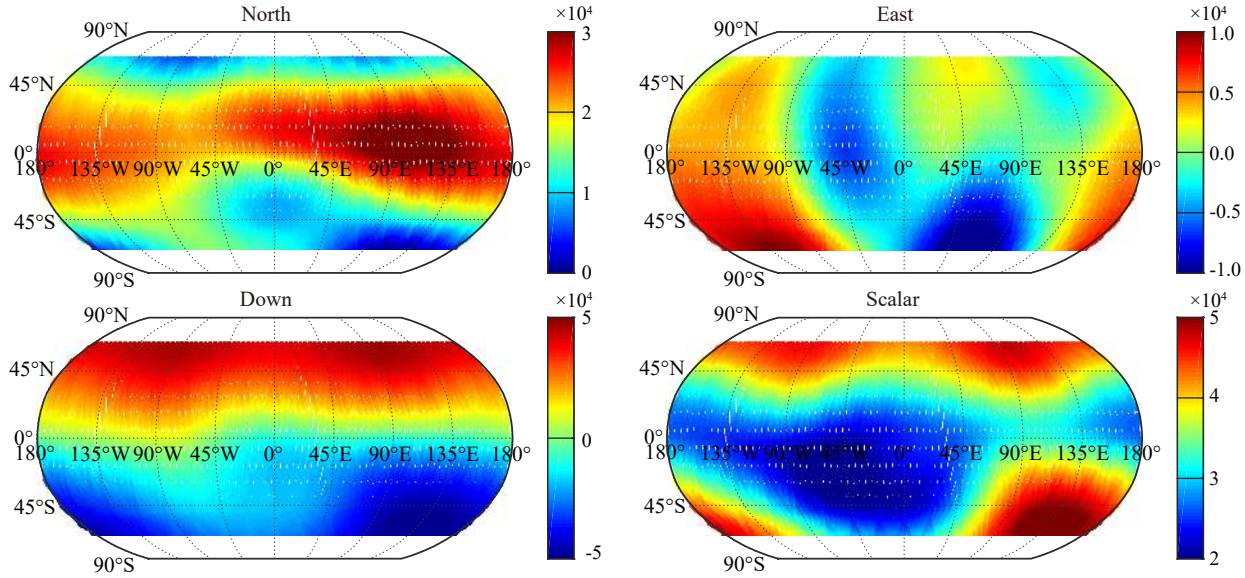

Figure 8. Geomagnetic field components (North, Ease and Down) and strength (Scalar) observed by CSES-HPM in a 5-day re-visiting period from May 19 to May 24 in 2018.

CHAOS, which is based on the observation data of Orsted, CHAMP, and SWARM satellites and combined with Earth's main magnetic model, lithospheric magnetic model, and ring current model (Olsen et al., 2006). Figure 9 and Table 4 show the comparison of the magnetic field as measured by CSES and by SWARM B during these 5 days. In middle and low latitude areas the consistency is good; in the areas around 45°N and 45°S the difference is larger. The main reason is that, on one hand, the transformation matrix to the star sensor is based on low latitude data; on the other hand, the high latitude area is more disturbed due to the currents in the polar regions. We put the comparison result and *Kp* index together for analysis, as shown in Figure 10, where the abscissa is the sum of the *Kp* index at the time of the two satellite ob-

Table 4. Comparison of HPM data and SWARM data

	For all intersections		For intersections below magnetic latitude 10°	
	Average	Variance	Average	Variance
North	6.09 nT	24.37 nT	–3.69 nT	9.13 nT
East	–6.12 nT	29.15 nT	–5.72 nT	21.26 nT
Down	–3.83 nT	12.36 nT	–8.91 nT	10.83 nT
Saclar	–1.35 nT	7.47 nT	–3.28 nT	7.62 nT
Angle	0.055°	0.041°	0.001°	0.0004°

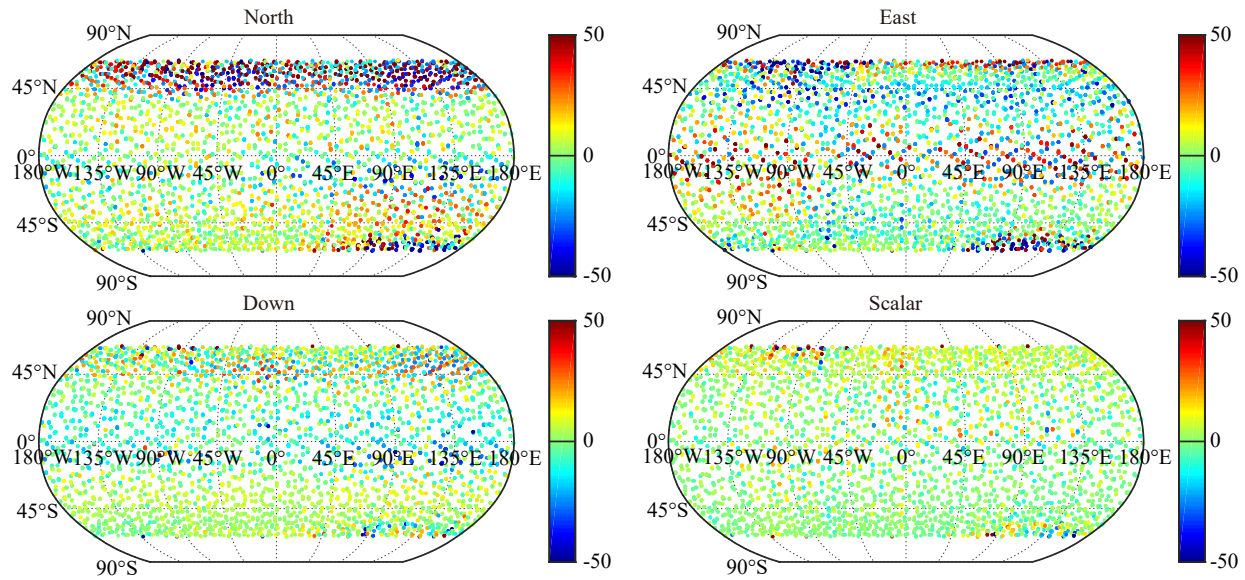

Figure 9. Magnetic field components (North, South and Down) and strength (Scalar) differences at orbit intersections between CSES and SWARM in May 19-24, 2018.

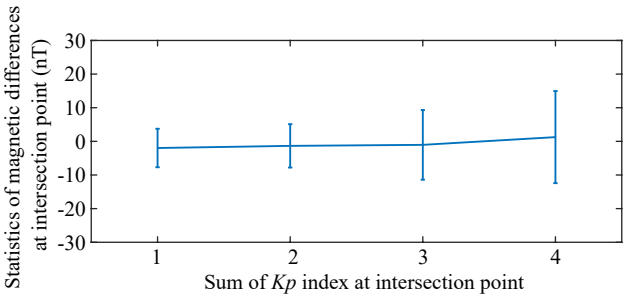

Figure 10. Variances of scalar magnetic field differences between CSES and SWARM increase with sum of *Kp* index at orbit intersections.

servations. It can be seen that with increasing *Kp* the variance of the difference between the two data sets increase, indicating that the CSES data and SWARM data are highly consistent.

4. Conclusion

Based on the in-orbit observation data, the ground calibration data of the CSES HPM, the characteristics of the FGM probes, CDSM probe, and satellite platform, we developed the data processing method. According to the processing results, the accuracy of scalar magnetic data is assessed to be 0.5 nT, while the accuracy of alignment is 0.05°, and the data are consistent with SWARM B data.

The current method is applicable to the first half year of CSES data after the satellite's launching. Referred to the experience of the SWARM satellite, some parameters may change after a long time in orbit due to impact of aspects of the space environment, such as solar radiation. After a certain time in orbit, we will analyze long-term CSES data and update our algorithm, which will further improve the quality of CSES magnetic exploration data.

The MAGSAT, CHAMP, and SWARM satellites are dedicated to magnetic field measurement. The accuracy of their vector magnetic field measurments reach respectively to 6 nT, 3 nT, and 1 nT (Mandea, 2006), which means that the pointing accuracy should be in the order of 0.001°. As a general-purpose electromagnetic field monitoring platform, CSES has not reached this level yet. So specific design is needed in the future to enhance the pointing accuracy of the platform.

Acknowledgments

This research made use of the data from CSES mission, a project funded by China National Space Administration (CNSA) and China Earthquake Administration (CEA). This research is supported by National Key Research and Development Program of China from MOST (2016YFB0501503).

References

Chen, S. W. (2009). Control and measure of satellite magnetic cleanliness. *Prog. Geophys* (*in Chinese*), *24*(2), 797–800. https://doi.org/10.3969/j.issn.1004-2903.2009.02.061

Cheng, B. J., Zhou, B., Magnes W, Lammegger, R., and Pollinger, A. (2018). High precision magnetometer for geomagnetic exploration onboard of the China Seismo-Electromagnetic Satellite. *Sci. China Technol. Sci.*, *61*(5), 659–668. https://doi.org/10.1007/s11431-018-9247-6

Friis-Christensen, E., Lühr, H., Hulot G. (2006). Swarm: A constellation to study the Earth's magnetic field. *Earth Planets Space*, *58*(4), 351–358. https://doi.org/10.1186/BF03351933

Lammegger, R. (2008). Method and device for measuring magnetic fields, WIPO, Patent WO/2008/151344.

Liu, J. C. and Zhu, Z. (2012). Explanation and Implementation of the IAU 2000/2006 Resolutions on Fundamental Astronomy. *Progr. Astron.* (*in Chinese*), *30*(4), 411–437.

Mandea, M. (2006). Magnetic Satellite Missions: Where have we been and where are we going?. *C. R. Geosci.*, *338*(14-15), 1002–1011. https://doi.org/10.1016/j.crte.2006.05.011

Merayo, J. M. G., Brauer, P., Primdahl, F., Petersen, J. R., and Nielsen, O. V. (2000). Scalar calibration of vector magnetometers. *Measur. Sci. Technol.*, *11*(2), 120–132. https://doi.org/10.1088/0957-0233/11/2/304

Olsen, N., Lühr, H., Mandea, M., Rother, M., Tøffner-Clausen, L., and Choi, S. (2006). CHAOS-a model of the Earth's magnetic field derived from CHAMP, Ørsted, and SAC-C magnetic satellite data. *Geophys. Int.*, *166*(1), 67–75. https://doi.org/10.1111/j.1365-246X.2006.02959.x

Olsen, N., Tøffner-Clausen, L., Sabaka, T. J., Brauer, P., Merayo, J. M. G., Jörgensen, J. L., Léger, J. M., Nielsen, O. V., Primdahl, F., and Risbo, T. (2003). Calibration of the Ørsted vector magnetometer. *Earth Planets Space*, *55*(1), 11–18. https://doi.org/10.1186/BF03352458

Pollinger, A., Lammegger, R., Magnes W, Hagen, C., Ellmeier, M., Jernej, I., Leichtfried, M., Kürbisch, C., Maierhofer, R., Baumjohann, W. (2018). Coupled Dark State Magnetometer for the China Seismo-Electromagnetic Satellite. *Measur. Sci. Technol.*, *29*(9). https://doi.org/10.108/1361-6501/aacde4

Potemra, T. A., Mobley, F. F., and Eckard, L. D. (1980). The geomagnetic field and its measurement: introduction and magnetic field satellite (Magsat) glossary. *APL Tech. Dig.*, *1*, 162–170.

Shen, X. H., Zhang, X. M., Yuan, S. G., Wang, L. W., Cao, J. B., Huang, J. P., Zhu, X. H., Piergiorgio, P., and Dai, J. P. (2018). The State-of-the-Art of the China Seismo-Electromagnetic Satellite Mission. *Sci. China Technol. Sci.*, *61*(5), 634–642. https://doi.org/10.1007/s11431-018-9242-0

Xiao, Q., Geng, X. L., Chen, J. G., Meng, L. F., Li, N., and Zhang, Y. J. (2018). Calibration methods of the interference magnetic field for Low Earth Orbit (LEO) magnetic satellite. *Chinese J. Geophys.* (*in Chinese*), *61*(8), 3134–3138. https://doi.org/10.6038/cjg2018L0408

Yin, F. (2010). *Mathematic Approaches for the Calibration of the CHAMP Satellite Magnetic Field Measurements*. Potsdam: Universität Potsdam.

Yin, F., Lühr, H., Rauberg, J., Michaelis, I., and Cai, H. T. (2013). Characterization of CHAMP magnetic data anomalies: magnetic contamination and measurement timing. *Measur. Sci. Technol.*, *24*(7), 445–455. https://doi.org/10.1088/0957-0233/24/7/075005

Zhang, Z. Q., Li, L., Zhou, B., and Zhang, Y. T. (2014). A method of in-orbit calibration of fluxgate magnetometer based on the measurement of absolute scalar magnetometer. *Satellite. Chin. Space Sci. Technol.* (*in Chinese*), *34*(2), 235–241. https://doi.org/10.11728/cjss2014.02.235

Zhou, B., Cheng, B. J., and Zhang, Y. T. (2018). The Earth magnetic field exploration mission of China seismo-electromagnetic satellite. *J. Remote Sens.* (*in Chinese*)(S1), 1993–2002. https://doi.org/10.11834/jrs.20187242

Zhou, B. and Wang, J. D. (2013). Influence of Magnetic Component Distribution of Satellite on Eliminating Remanant Magnetic Field by Gradient Method. *Chin. Space Science and Technology* (*in Chinese*), *33*(5), 29–34. https://doi.org/10.3780/j.issn.1000-758X.2013.05.005